PAPER

Ag$_2$Mo$_2$O$_7$: an oxide solid-state Ag$^+$ electrolyte†

Weixin Yan,[a] Dongmei Zhu,[a] Zhaofeng Wang,[a] Yunhao Xia,[a] Dong-Yun Gui,[b] Fa Luo[a] and Chun-Hai Wang [ID] *[ac]

Ag$_2$Mo$_2$O$_7$ powders and micro-crystals were prepared at 400 °C for 24 h and 500 °C for 6 h using solid-state reactions. The Ag$_2$Mo$_2$O$_7$ samples crystalized in a triclinic $P\bar{1}$ space group with the cell parameters a = 6.0972(1) Å, b = 7.5073(1) Å, c = 7.6779(2) Å, α = 110.43(1)°, β = 93.17(1)°, γ = 113.51(1)°, and V = 294.17(1) Å^3 from Rietveld refinements. Ag$_2$Mo$_2$O$_7$ powder is homogeneous with size of 2–8 μm and the ceramic pellets are in good sintering conditions with a relative density ~93%. The indirect band gaps E_g(i) of Ag$_2$Mo$_2$O$_7$ from reflectance measurements and DFT calculations are 2.63(1) and 1.80 eV. The vibrational modes of Ag$_2$Mo$_2$O$_7$ were investigated by first-principles (DFT) calculations and Raman spectrum measurements with 24 of 33 predicted Raman modes recorded. According to DOS analyses, the valence bands (VB) of Ag$_2$Mo$_2$O$_7$ are mainly constituted of O-2p and Ag-4d orbitals, while the conduction bands (CB) are mainly composed of Mo-4d and the O-2p orbitals. Regarding the impedance analysis, Ag$_2$Mo$_2$O$_7$ is a silver oxide ion electrolyte with a conductivity of ~5 × 10^{-4} S cm^{-1} at 450 °C. The carrier activation energy of Ag$_2$Mo$_2$O$_7$ is 0.88(3) eV from the temperature dependent conductivity measurements.

Introduction

The solid-state electrolyte (SSE) is a kind of solid or quasi-solid material with high ionic conductivity (and generally low electronic conductivity) at room or high temperatures.[1–3] Solid-state electrolytes are widely used in battery, electrolysis and sensor applications. SSEs can be categorized into inorganic solid-state electrolytes, polymer solid-state electrolytes and composite solid-state electrolytes.[4–6] Regarding the charge carriers, there are several well-known SSE materials, such as lithium ion SSEs (*e.g.* Li$_3$N, Li$_{3x}$La$_{(2/3)-x}$TiO$_3$, Li$_7$La$_3$Zr$_2$O$_{12}$),[7–9] sodium ion SSEs (*e.g.* NASICON, β-Al$_2$O$_3$),[10,11] oxygen ion SSEs [*e.g.* yttria-stabilized zirconia (YSZ), gadolinium doped ceria (GDC), Bi$_4$V$_2$O$_{11}$],[12–14] proton SSEs (*e.g.* NAFION),[15] and silver ion SSEs (*e.g.* AgI).[16] Though Ag is a heavy element, the ionic radii and polarizable electron shells make Ag$^+$ suitable for fast ion transport.[17] More than 100 years ago, the very first Ag$^+$ SSE silver iodide (α-AgI) was investigated by Turbandt and Lorenz.[18] Owens and Argue observed the highest Ag$^+$ ionic conductivity in KAg$_4$I$_5$ and RbAg$_4$I$_5$ with a conductivity σ of 0.21 cm^{-1} at 20 °C, respectively. They also reported that the conductivities are contributed by Ag$^+$.[19] To date, most Ag$^+$ electrolytes

investigated are limited in halides especially iodide. As oxides are very common in studies and shows significant chemistry difference with iodide, it is important to study the possible oxide solid-state Ag$^+$ electrolyte to investigate the mechanism of oxide SSE and develop new SSE, which is critical in the study of related solid-state devices.

Sliver dimolybdate, Ag$_2$Mo$_2$O$_7$, was found in the fused salt Ag$_2$MoO$_4$–MoO$_3$ using X-ray diffraction techniques by Gate-house. Ag$_2$Mo$_2$O$_7$ shows a triclinic symmetry (space group $P\bar{1}$) with cell parameters[20] a = 6.11(2) Å, b = 7.49(2) Å, c = 7.66(2) Å, α = 109.8°, β = 93.5°, γ = 113.6°. Ag$_2$Mo$_2$O$_7$ with an indirect band gap E_g of 2.65 eV,[21] has been widely investigated in various applications, such as catalysts,[22] antibacterial material,[23] microwave applications[24] and fuel cells.[25] Zhang investigated Ag$_2$Mo$_2$O$_7$ as an anode for lithium-ion batteries and observed a high specific capacity (discharge capacity of 825 mA h g^{-1} with capacity retention of 95% over 100 cycles) and superior rate capability (discharge capacity of 263 mA h g^{-1} at the high current density of 2 A g^{-1}).[26] Considering the crystal structure, Ag$_2$Mo$_2$O$_7$ might be an oxide solid-state electrolyte in our experiences. To date, there is no studies reported on the conductivity and charge carries of Ag$_2$Mo$_2$O$_7$ to our knowledge.

Generally, an ideal electrolyte is expected to give a high ionic conductivity and a low electronic conductivity, which should be an electronic insulator or semiconductor with ion migrations in physics. The electronic properties of solid-state materials are defined by electronic orbitals and band structures (including the density of state, DOS). The ion migration is confined by atomic vibrations and phonons. Thus, the study on the band

[a]*State Key Laboratory of Solidification Processing, Northwestern Polytechnical University, Xi'an, Shaanxi 710072, China. E-mail: chwang81@gmail.com*

[b]*Institute of Functional Materials, College of Materials Science and Engineering, Xi'an University of Architecture and Technology, Xi'an, Shaanxi 710055, China*

[c]*School of Chemistry, The University of Sydney, Sydney, NSW 2006, Australia*

† Electronic supplementary information (ESI) available. See DOI: 10.1039/d1ra07097e

structure (DOS and band gap) and phonons (vibrational modes) is important for the knowledge of solid-state electrolytes. To our knowledge, there is no studies reported on the band structures and vibrational modes of $Ag_2Mo_2O_7$.

In this study, we synthesized $Ag_2Mo_2O_7$ samples through solid-state reaction method and investigated the crystal structure of $Ag_2Mo_2O_7$ by single crystal and powder X-ray diffractions and first-principle calculations. We also studied the vibrational modes, band structures, Raman spectra, diffuse reflectance, ionic conductivity and charge carriers of $Ag_2Mo_2O_7$ in details.

Experimental procedures and calculation details

Synthesis

The $Ag_2Mo_2O_7$ powder and microcrystal samples were prepared by the high temperature solid-state reaction method. Stoichiometric Ag_2O and MoO_3 (99.99%, Macklin, dried at 300 °C before use) were weighed and ground using an agate pestle and mortar. The mixture was then calcined at 400 °C for 24 h with an intermediate ground. After calcination, bright yellow $Ag_2Mo_2O_7$ powder sample was synthesized according to the XRD analysis. The $Ag_2Mo_2O_7$ powder was added with polyvinyl alcohol (PVA, 5 wt%) as binder and uniaxially pressed into pellets (thickness ~1 mm) with a Φ15 mm die at about 120 MPa. The pressed pellets were heated at 400 °C for 1 h to drive off the PVA and sintered at 480 °C for 6 h with a ramp of 5 °C min^{-1} (both heat up and cool down). The sintered samples ($Ag_2Mo_2O_7$ ceramics) were then carefully polished with sandpapers. The density of ceramics was determined using the Archimedes method. For the growth of $Ag_2Mo_2O_7$ micro-crystals, $Ag_2Mo_2O_7$ powder was heated at 500 °C for 6 h.

Measurements

The phase of $Ag_2Mo_2O_7$ samples was analyzed using powder X-ray diffraction (PXRD) (miniFlex 600, Rigaku, Cu-Kα) in 2θ range of 5–120° with a scanning rate 2° min^{-1} at room temperature. The single crystal X-ray diffraction (SXRD) data of a micro single crystal (20 × 10 × 10 μm) were collected by a Rigaku XtaLAB Synergy-R (Cu-Kα) diffractometer at 150 K (−123 °C). A total of 7725 frames were recorded at 7 s per frame. The crystal structure of $Ag_2Mo_2O_7$ was analyzed by Jana 2006 [27] and TOPAS Academic (TA)[28] and finally obtained by the Rietveld refinements against PXRD data measured. The crystal structure visualization was done using VESTA.[29] The microstructure of the samples was observed by a scanning electron microscope (SEM, Tescan Vega3 SBH, Brno, Czech Republic). The Raman spectrum collected on a pellet sample by a Raman spectrometric analyzer (Renishaw inVia, Britain) in 100–1200 cm^{-1} with the resolution ~2 cm^{-1}, excited by a 532 nm laser. The conductivity of $Ag_2Mo_2O_7$ pellets was measured by an electrochemical workstation (CHI 660e, Chenhua) at different temperatures. The Ag electrode was prepared by heated the covered silver paste at 400 °C for 2 h and the Au electrode was made by ion sputter coating.

Calculations

The band structure and vibrational modes of $Ag_2Mo_2O_7$ was calculated using the CASTEP software package based on the density functional theory (DFT).[30] The plane wave basis was used for the expansion of the valence-electron wave functions based on generalized gradient approximation (GGA). The energy cutoff of plane wave basis was set to 1020 eV, and the criterion for self-consistency was set as eigen-energy within 10^{-10} eV per atom. The Brillouin zone sampling set (*k*-points) was 6 × 5 × 5 Monkhorst–Pack grid (reciprocal spacing ~0.03 $Å^{-1}$) and the pseudopotential (PBEsol) was constructed from the CASTEP database. $Ag_2Mo_2O_7$ crystal structure obtained from the XRD analysis in this work was selected as original model and a further geometry optimization was run with convergence tolerance 10^{-9} eV per atom. The band structure and vibrational modes of the optimized $Ag_2Mo_2O_7$ model were then calculated. The vibrational modes were calculated using linear response method[31] with the convergence tolerance 10^{-5} eV $Å^{-2}$.

Results and discussions

Samples and microstructures

With the optimized synthesis described in the experimental section, desired $Ag_2Mo_2O_7$ samples (powder, micro-crystal, and ceramics) were successfully synthesized. All the samples are bright yellow and there is no any impurity observed from XRD analysis. The microstructure of $Ag_2Mo_2O_7$ powders, micro-crystals and ceramics (fractured surface) observed by SEM are shown in Fig. 1a–c. The fine $Ag_2Mo_2O_7$ powder is obtained after the calcination at 400 °C with the particle size in 2–8 μm (Fig. 1a). The particles grew significantly to ~20 μm (Fig. 1b) after heated at 500 °C for 6 h and most of the particles are single-domain micro-crystals from our single crystal diffraction analysis. The ceramic samples prepared are well sintered with a relative density of ~93% and a grain size of 20–100 μm (Fig. 1c). Some pores distributed in the grains and grain boundaries should be caused by the fire out of the PVA binders. However, there is no any obvious voids or cracks in the sample, which is in consistent with the high relative density measured.

Crystal structure of $Ag_2Mo_2O_7$

The single-crystal X-ray diffraction data (SXRD) of $Ag_2Mo_2O_7$ at 150 K were collected through a full reciprocal sphere with the resolution 0.8 Å to check the symmetry and space group. The observed reflections were well-indexed with the triclinic unit cell ($P\bar{1}$) $a = 6.0907(4)$ Å, $b = 7.4593(4)$ Å, $c = 7.6668(5)$ Å, $\alpha = 110.370(5)°$, $\beta = 93.336(5)°$, $\gamma = 113.610(5)°$, $V = 291.18(4)$ $Å^3$. By charge-flipping analysis and refinements, the crystal structure of $Ag_2Mo_2O_7$ was obtained and a fairly good agreement was achieved with weighted residual factors (R_{wp}) of 0.054.

The XRD pattern of $Ag_2Mo_2O_7$ powder (PXRD) sample at room temperature is shown in Fig. 1e. The pattern is in a reliable quality with the highest reflection >35 000 counts. Rietveld refinements of the $Ag_2Mo_2O_7$ structure model obtained from SXRD against the PXRD data were carried out to obtain a higher

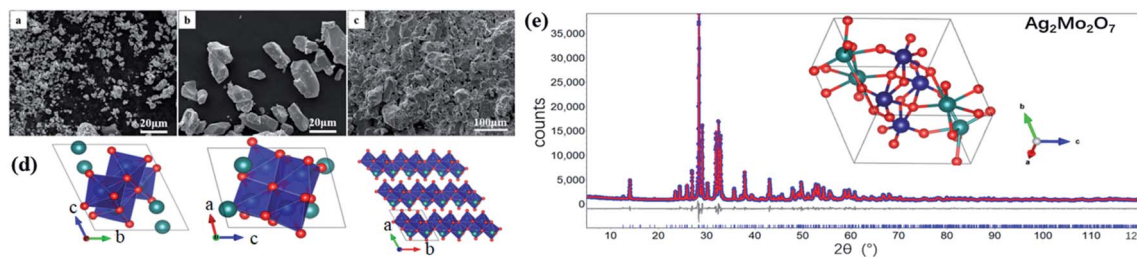**Fig. 1** SEM images of $Ag_2Mo_2O_7$ (a) powders, (b) micro-crystals, (c) fractured surface of a ceramic pellet samples; (d) representation of the crystal structure of $Ag_2Mo_2O_7$ from a, b and c directions. Silver ions (green), molybdenum (navy), oxygen ions (red); (e) XRD patterns, Rietveld refinements and crystal structure of $Ag_2Mo_2O_7$, circle points: observed, red solid line: calculated curve, solid line below the data: the difference curve, vertical tick marks: peak positions.

accuracy. In the refinements, background, zero shift, peak profile, the cell parameters, atomic coordinates, and atomic displacement parameters (ADPs) were refined. An excellent agreement between the diffraction data and the prediction from the structure model is achieved with the weighted residual factor (R_{wp}) $\sim$0.064. The refined profile is shown in Fig. 1d and the refined crystal structure is presented in Fig. 1e. Details of the refined structure is shown in Table 1 and given in the crystallographic information files (CIF) in the ESI.† All the reflections observed can be indexed in the refinements, which means the impurities is in a very low level. The cell parameters from the PXRD analysis are $a = 6.0972(1)$ Å, $b = 7.5073(1)$ Å, $c = 7.6779(2)$ Å, $\alpha = 110.43(1)°$, $\beta = 93.17(1)°$, $\gamma = 113.51(1)°$, $V = 294.17(1)$ Å^3, which are slight larger than that from SXRD analysis. This should be caused by the thermal expansions due to the different temperature in the measurements. The refined parameters here agree with the reported ones[32] $a = 6.095(1)$ Å, $b = 7.501(1)$ Å, $c = 7.681(1)$ Å, $\alpha = 110.4(1)°$, $\beta = 93.3(1)°$, $\gamma = 113.5(1)°$. $V = 294.37(4)$ Å^3. In the crystal structure of $Ag_2Mo_2O_7$, edge-shared MoO_6 octahedra form chains along axis a and the Ag^+ ions sit between the chains. The distance between neighboring Ag^+ is $\sim$3.575(6) Å. Thus, it is possible for the Ag^+ to migrate along axis a from crystallographic view and $Ag_2Mo_2O_7$ should be a potential oxide Ag^+ electrolyte.

Raman spectrum

There are 22 atoms ($Z = 2$) in a $Ag_2Mo_2O_7$ primitive cell, which gives 66 vibrational modes with 3 acoustic modes and 63 optical modes. According to group theory,[33] the vibrational modes (acoustic modes $\Gamma_{acoustic}$ and optical modes $\Gamma_{optical}$) of $Ag_2Mo_2O_7$ are

$$\Gamma_{acoustic} = 3A_u \tag{1}$$

$$\Gamma_{optical} = 33A_g + 30A_u \tag{2}$$

Of the optical modes, A_g are Raman active and A_u are IR active. Thus, there are a total of 30 IR-active modes $\Gamma_{IR} = 30A_u$, and 33 Raman-active modes $\Gamma_{Raman} = 33A_g$.

The Raman spectrum of $Ag_2Mo_2O_7$ measured is shown in Fig. 2. 24 of the 33 predicted first-order Raman modes can be clearly recognized. By peak fitting using Voigt profile, the frequency, intensity, and peak width (full width at half

Table 1 Details of the crystal structure of $Ag_2Mo_2O_7$

Space group	$P\bar{1}$ (2)
PXRD	
a (Å)	6.0972(1)
b (Å)	7.5073(1)
c (Å)	7.6779(1)
α (°)	110.42(1)
β (°)	93.16(1)
γ (°)	113.50(1)
V (Å^3)	294.2(2)
d_{theory} (g cm^{-3})	5.866(1)

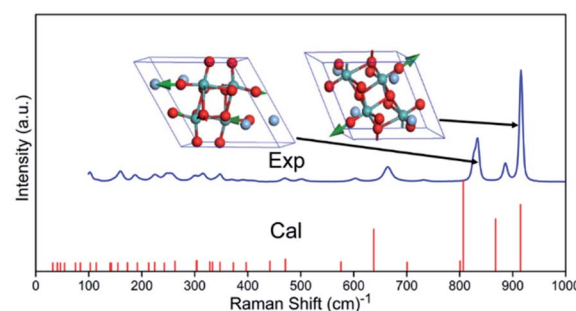|	x	y	z	U_{iso} (Å^2)
Ag1	0.7813(6)	0.2741(5)	0.2674(4)	0.0066(2)
Ag2	0.2312(7)	0.2397(5)	0.0370(5)	0.0073(2)
Mo1	0.6698(6)	0.1706(5)	0.7490(5)	0.0005(2)
Mo2	0.7580(7)	0.7710(6)	0.4541(5)	0.0003(2)
O1	0.603(3)	0.505(3)	0.278(3)	0.0066(13)
O2	0.774(4)	0.112(3)	0.939(3)	0.0066(13)
O3	0.362(4)	0.140(3)	0.766(3)	0.0040(12)
O4	0.490(3)	0.834(3)	0.519(3)	0.0015(11)
O5	0.921(4)	0.115(3)	0.600(3)	0.0029(12)
O6	0.870(4)	0.759(3)	0.656(3)	0.0074(13)
O7	0.843(4)	0.429(3)	0.821(2)	0.0057(13)

Fig. 2 Raman spectra of $Ag_2Mo_2O_7$. Exp.: measured, Cal.: calculated. Two Raman modes with highest intensity from DFT calculations are shown as inset.

© 2022 The Author(s). Published by the Royal Society of Chemistry

maximum, FWHM) of recognized modes are obtained and listed in Table S1 which is shown in ESI.† The detailed fit profiles are also shown as Fig. S1 in ESI,† which shows excellent agreements from the fit.

Diffuse reflectance

The optical band gap and absorption coefficient of semiconductor can be calculated by the equation[34]

$$(\alpha h\nu)^n = K(h\nu - E_g)$$

where α is the linear absorption coefficient of the material, $h\nu$ is the photon energy, K is a proportionality constant, E_g is the optical band gap, and n is a constant associated with different kinds of electronic transitions ($n = 1/2$ for a direct allowed, $n = 2$ for an indirect allowed). The $(\alpha h\nu)^n - h\nu$ curve of $Ag_2Mo_2O_7$ are calculated from diffuse reflectance measurements and plotted in Fig. 3a. $Ag_2Mo_2O_7$ shows an indirect band gap $E_g(i) = 2.63(1)$ eV and direct band gap $E_g(d) = 2.71(1)$ eV.

Band structures

After DFT geometry optimization, the cell parameters of the optimized structure show excellent agreements (difference of cell parameter <1%) with the one from our Rietveld refinements. The band structures of $Ag_2Mo_2O_7$ calculated is plotted in Fig. 3b. $Ag_2Mo_2O_7$ gives an indirect band gap of $E_g(i) = 1.80$ eV ($F \rightarrow Z$) and a direct band gap of $E_g(d) = 1.88$ eV ($Z \rightarrow Z$). This is slight smaller than the experimental results from diffuse reflectance analysis. In general, DFT calculations often underestimate the band gaps of solids, especially for semiconductors.[35,36]

The partial density of state (PDOS) plots for different atoms and total density of state (DOS) of $Ag_2Mo_2O_7$ are shown in Fig. S2 in ESI.† In the vicinity of the Fermi level, the main contribution to the valence bands (VB) is from the O-2p and Ag-4d orbitals, while the conduction bands (CB) are formed mainly by the Mo-4d and O-2p orbitals.

Vibrational modes

The eigenfrequency and intensity of the optical vibrational modes of $Ag_2Mo_2O_7$ calculated are listed in Table S2 (Raman modes) and Table S3 (infrared modes) of ESI.† Refers to the theoretical intensity, we give the assignment of the observed Raman modes reliably, which are also given in Table S2.† For the Raman modes, the frequency of vibrational modes from DFT calculations (theoretical) is lower than that from measured spectra (experimental), which agrees with the general results from our previous studies.[37] The vibration detail (vector of atomic motions) of five IR and Raman vibrational modes with high intensities is given as Fig. S3 and S4.†

According to the atomic motion of vibrational modes, vibrations of O^{2-} contribute to all the vibrational modes of $Ag_2Mo_2O_7$. Generally, the vibrational modes with eigenfrequency $f \geq 195.52$ cm^{-1} are dominated by the vibrations of O^{2-} (light atom vibrations). The vibrations of Ag^+ and Mo^{6+} mainly contribute to the vibrational modes at 126.84 cm$^{-1} \leq f \leq 195.52$ cm^{-1} and 32.01 cm$^{-1} \leq f \leq 126.84$ cm^{-1}. The vibrational modes (phonons) of Ag^+ give a rather low eigenfrequencies. As the frequency f of a vibration is determined by the restoring force k and the reduced mass m^* ($f \propto k/m^*$). Thus, the restoring force k and the bonding of Ag^+ in $Ag_2Mo_2O_7$ is weak, which makes it easy to be activated for migration at a low or intermediate temperature.

Ionic conductivity

The conductivity of samples was determined by impedance analysis in the frequency range 0.1 Hz to 10^6 Hz. Two different electrodes (Au and Ag) were used to determine the species of charge carries in $Ag_2Mo_2O_7$ and the Nyquist plots are shown in Fig. 3c. An obvious Warburg tail is observed for sample with Au electrodes, but disappeared for sample with Ag electrodes. This indicates the charge carries of $Ag_2Mo_2O_7$ ceramics should be Ag^+. As discussed in crystal structure of $Ag_2Mo_2O_7$, the Ag^+ sits between the Mo–O octahedra chains, which makes it possible for the migration of Ag^+ in the structures. Resistance difference between gold electrode
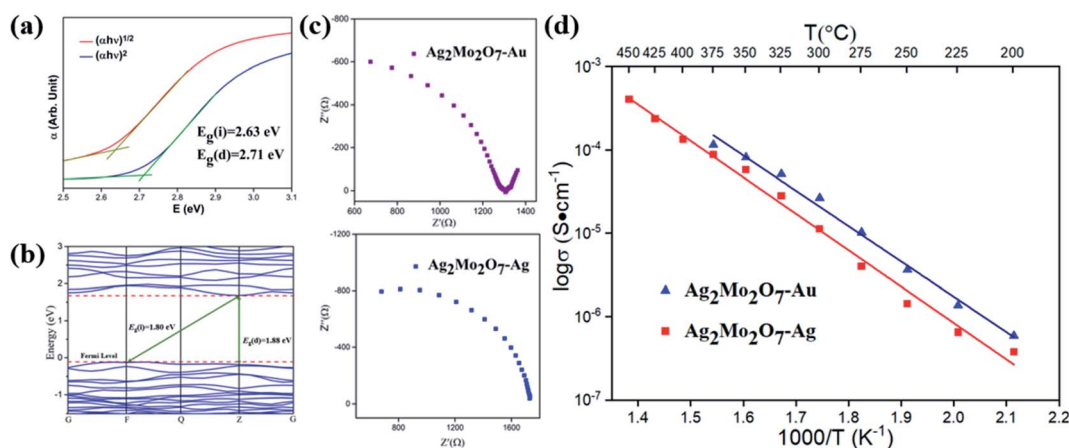

Fig. 3 (a) $(\alpha h\nu)^n - h\nu$ curve of $Ag_2Mo_2O_7$ from diffuse reflectance measurements; (b) band structure and density of state (DOS) of $Ag_2Mo_2O_7$. The Fermi level is set as $E_{Femi} = 0$ eV; (c)Nyquist plot (impedance) of $Ag_2Mo_2O_7$ with two different electrodes at 325 °C; (d) temperature dependent conductivity of $Ag_2Mo_2O_7$ with two different electrodes.

and sliver electrode is derived from the sample size and ceramic-electrode contact.

For non-metal conductors, the conductivity σ of a non-metal system follows the Arrhenius equation[38]

$$\sigma = \sigma_0 \exp\left(-\frac{E_a}{kT}\right)$$

where E_a is the activation energy of charge carriers, k is the Boltzmann constant and T is the absolute temperature. The temperature dependent conductivity of $Ag_2Mo_2O_7$ with Ag as electrodes is plotted in Fig. 3d. As expected, the conductivity of $Ag_2Mo_2O_7$ increases as the temperature increases and σ reaches a level of $\sim 5 \times 10^{-4}$ S cm^{-1} at 450 °C (Ag). The conductivity of sample with Au electrode is slightly higher than that of sample with Ag electrode, this should be caused by the contact between electrodes and samples. The Au electrodes made by sputtering should give a better contact than that of Ag electrode made by paste coating. The $\sigma - T$ data agree with the Arrhenius equation and the activation energy E_a of charge carriers in $Ag_2Mo_2O_7$ is estimated to be 0.88(3) eV. As E_a of Ag^+ is much smaller than the electron band gap E_g [$\sim$2.63(1) eV], the conductivity of $Ag_2Mo_2O_7$ should be dominated by the Ag^+. However, the Ag^+ conductivity in the oxide $Ag_2Mo_2O_7$ is much lower than that of iodide Ag^+ electrolyte, which means the interaction between Ag^+ and the matrix in $Ag_2Mo_2O_7$ oxide is still too strong compare with the iodide. A modification such as doping and substitution to optimise the interactions should be an effective way to improve the Ag^+ conductivities.

Conclusions

$Ag_2Mo_2O_7$ powder with a particle size of 2–8 μm have been synthesized by conventional solid-state reaction. The crystal structure of $Ag_2Mo_2O_7$ is in a triclinic $P\bar{1}$ space group, with the cell parameters $a = 6.0972(1)$ Å, $b = 7.5073(1)$ Å, $c = 7.6779(2)$ Å, $\alpha = 110.43(1)°$, $\beta = 93.17(1)°$, $\gamma = 113.51(1)°$, $V = 294.17(1)$ Å^3. The band gap of $Ag_2Mo_2O_7$ is estimated to be indirect band gap $E_g(i) = 2.63(1)$ eV and direct band gap $E_g(d) = 2.71(1)$ eV. The VB are mainly contributed by O-2p and Ag-4d orbitals, while the CB is dominated by the Mo-4d and the O-2p orbitals. 24 of the 33 predicted first-order Raman modes were recognized and assigned in the Raman spectrum. The vibrational modes with $f \geq$ 195.52 cm^{-1} are dominated by the vibrations of O^{2-} (light atom vibrations). The Ag^+ and Mo^{6+} mainly contributed to the vibrational modes at 126.84 cm$^{-1} \leq f \leq$ 195.52 cm^{-1} and 32.01 cm^{-1} $\leq f \leq$ 126.84 cm^{-1}. $Ag_2Mo_2O_7$ is a Ag^+ solid state electrolyte with the activation energy E_a estimated to be 0.88(3) eV. The Ag^+ conductivity of $Ag_2Mo_2O_7$ is >5 × 10^{-4} S cm^{-1} at 450 °C.

Conflicts of interest

There are no conflicts to declare.

Acknowledgements

Notes and references

1 Z. Zhang, Y. Shao, B. Lotsch, Y.-S. Hu, H. Li, J. Janek, L. F. Nazar, C.-W. Nan, J. Maier, M. Armand and L. Chen, *Energy Environ. Sci.*, 2018, **11**, 1945–1976.

2 Z. G. G. Yang, J. W. Stevenson and P. Singh, *Adv. Mater. Processes*, 2003, **161**, 34–37.

3 O. Z. Sharaf and M. F. Orhan, *Renew. Sust. Energ. Rev.*, 2014, **32**, 810–853.

4 Z. Gao, L. V. Mogni, E. C. Miller, J. G. Railsback and S. A. Barnett, *Energy Environ. Sci.*, 2016, **9**, 1602–1644.

5 W. H. Kan, A. J. Samson and V. Thangadurai, *J. Mater. Chem. A*, 2016, **4**, 17913–17932.

6 J. B. Lu, Z. T. Zhang and Z. L. Tang, *Rare Met. Mater. Eng.*, 2005, **34**, 1177–1180.

7 Y. Heng, W. Wang, Q. Li, X. Li, M. Dai, C. Yu, Z. Xue, J. Xia, G. Zhou and D. Jiang, *J. Electroceram.*, 2021, 1–8.

8 Y. Ren, S. Yang, X. Ma, C. Zhang, B. Song, C. Sun, X. Tan and S. Sun, *Appl. Surf. Sci.*, 2021, **567**, 150746.

9 J. C. Verduzco, E. E. Marinero and A. Strachan, *Integr. Mater. Manuf. Innov.*, 2021, **10**, 299–310.

10 M. Hou, X. Yang, F. Liang, P. Dong, Y. Chen, J. Li, K. Chen, Y. Dai and D. Xue, *ACS Appl. Mater. Interfaces*, 2021, **13**, 33262–33271.

11 J. R. Walker and C. R. A. Catlow, *J. Phys. C: Solid State Phys.*, 1982, **15**, 6151–6161.

12 V. V. Kharton, A. V. Kovalevsky, A. P. Viskup, F. M. Figueiredo, A. A. Yaremchenko, E. N. Naumovich and F. M. B. Marques, *J. Eur. Ceram. Soc.*, 2001, **21**, 1763–1767.

13 V. Sharma, A. K. Shukla and J. Gopalakrishnan, *Solid State Ionics*, 1992, **58**, 359–362.

14 M. J. Son, M. W. Kim, A. V. Virkar and H.-T. Lim, *Electrochim. Acta*, 2020, **353**, 136450.

15 H. Gao and K. Lian, *RSC Adv.*, 2014, **4**, 33091–33113.

16 M. C. R. Shastry and K. J. Rao, *Solid State Ionics*, 1992, **51**, 311–316.

17 D. W. Kim, I.-S. Cho, S. Lee, S.-T. Bae, S. S. Shin, G. S. Han, H. S. Jung and K. S. Hong, *J. Am. Ceram. Soc.*, 2010, **93**, 3867–3872.

18 C. Tubandt and E. Lorenz, *Z. Phys. Chem.*, 1914, **24**, 513–543.

19 B. B. Owens and G. R. Argue, *Science*, 1967, **157**, 308–310.

20 B. M. Gatehouse and P. Leverett, *J. Chem. Soc. D*, 1970, **1**, 484–496.

21 M. Hashim, C. Hu, Y. Chen, C. Zhang, Y. Xi and J. Xu, *Phys. Status Solidi A*, 2011, **208**, 1937–1941.

22 S. A. Driscoll and U. S. Ozkan, *Stud Surf Sci Catal*, 1994, **82**, 367–375.

23 H. Tang, A. Lu, L. Li, W. Zhou, Z. Xie and L. Zhang, *Chem. Eng. J.*, 2013, **234**, 124–131.

24 L. G. Vanuitert and S. Preziosi, *J. Appl. Phys.*, 1962, **33**, 2908–2909.

25 V. V. Kharton, F. M. B. Marques and A. Atkinson, *Solid State Ionics*, 2004, **174**, 135–149.

26 M. Zhang, Y. Gao, N. Chen, X. Ge, H. Chen, Y. Wei, F. Du, G. Chen and C. Wang, *Chem.–Eur. J.*, 2017, **23**, 5148–5153.

27 V. Petricek, M. Dusek and L. Palatinus, *Z. Krist-cryst. Mater.*, 2014, **229**, 345–352.

28 A. A. Coelho, J. S. O. Evans, I. R. Evans, A. Kern and S. Parsons, *Powder. Diffr.*, 2011, **26**, S22–S25.

29 K. Momma and F. Izumi, *J. Appl. Crystallogr.*, 2011, **44**, 1272–1276.

30 V. Milman, K. Refson, S. J. Clark, C. J. Pickard and J. R. Yates, *J. Mol. Struct.: THEOCHEM*, 2010, **954**, 22–35.

31 K. Refson, P. R. Tulip and S. J. Clark, *Phys. Rev. B: Condens. Matter Mater. Phys.*, 2006, **73**, 155114.

32 B. M. Gatehouse and P. Leverett, *J. Chem. Soc., Dalton Trans.*, 1976, 1316–1320.

33 D. M. P. Mingos, *Nat. Phys. Sci.*, 1972, **236**, 99–102.

34 T. J. Farrell, M. S. Patterson and B. Wilson, *Med. Phys.*, 1992, **19**, 879–888.

35 A. Seidl, A. Gorling, P. Vogl, J. A. Majewski and M. Levy, *Phys. Rev. B: Condens. Matter Mater. Phys.*, 1996, **53**, 3764–3774.

36 H. Xiao, J. Tahir-Kheli and W. A. Goddard III, *J. Phys. Chem. Lett.*, 2011, **2**, 212–217.

37 C.-H. Wang, W. Shu, Y. Qing, F. Luo, D. Zhu and W. Zhou, *J. Am. Ceram. Soc.*, 2021, **104**, 1797–1805.

38 M. D. Archer, *ACS Symp. Ser.*, 1989, **390**, 115–126.